Remote Sensing of Environment 114 (2010) 2026–2035

Contents lists available at ScienceDirect

Remote Sensing of Environment

journal homepage: www.elsevier.com/locate/rse

Dark-spot detection from SAR intensity imagery with spatial density thresholding for oil-spill monitoring

Yuanming Shu, Jonathan Li *, Hamad Yousif, Gary Gomes

Department of Geography and Environmental Management, Faculty of Environment, University of Waterloo, 200 University Avenue West, Waterloo, Ontario, Canada N2L 3G1

ARTICLE INFO

Article history:
Received 8 October 2009
Received in revised form 16 April 2010
Accepted 17 April 2010

Keywords:
Oil spill
Dark-spot detection
Intensity threshold
Spatial density threshold
Density estimation

ABSTRACT

Dark-spot detection is a critical and fundamental step in marine oil-spill detection and monitoring. In this paper, a novel approach for automated dark-spot detection using synthetic aperture radar (SAR) intensity imagery is presented. The key to the approach is making use of a spatial density feature to differentiate between dark spots and the background. A detection window is passed through the entire SAR image. First, intensity threshold segmentation is applied to each window. Pixels with intensities below the threshold are regarded as potential dark-spot pixels while the others are potential background pixels. Second, the density of potential background pixels is estimated using kernel density estimation within each window. Pixels with densities below a certain threshold are the real dark-spot pixels. Third, an area threshold and a contrast threshold are used to eliminate any remaining false targets. In the last step, the individual detection results are mosaicked to produce the final result. The proposed approach was tested on 60 RADARSAT-1 ScanSAR intensity images which contain verified oil-spill anomalies. The same parameters were used in all tests. For the overall dataset, the average of commission error, omission error, and average difference were 7.0%, 6.1%, and 0.4 pixels, respectively. The average number of false alarms was 0.5 per unit image and the average computational time for a detection window was 1.2 s using a PC-based MATLAB platform. Our experimental results demonstrate that the proposed approach is fast, robust and effective.

1. Introduction

Marine oil pollution, caused by discharges from ships, and leakages from oil platforms and oil-tanker accidents, is a major threat to fragile marine and coastal ecosystems. Efficient monitoring and early warning are essential to prevent widespread damage from oil pollution and to reduce its adverse impact on ecosystems. The combined use of satellite and aircraft surveillance flights is a cost-effective means of achieving this goal. Satellite monitoring helps identify potential locations of oil pollution over large areas, while aircraft patrols help verify actual oil spills and provide evidence to apprehend polluters. The synthetic aperture radar (SAR)-equipped satellites are often preferred to optical ones, as they are independent of sunlight and not affected by clouds. The commonly used SAR sensors for oil-spill monitoring include RADARSAT-1, ENVISAT and ERS-2 (Brekke & Solberg, 2005; Topouzelis, 2008).

The detectability of oil spills using SAR sensors relies on the fact that oil slicks dampen the wind-generated, short gravity-capillary waves and reduce backscattering from the sea surface. This results in dark regions on SAR imagery which contrast with the surrounding water surfaces (Brekke & Solberg, 2005; Topouzelis, 2008). A major problem is that other ocean phenomena may also generate dark regions which are known as look-alikes. Examples are low-wind areas, organic films, areas of wind-shadow near coasts, rain cells, shear zones caused by currents, grease ice, internal waves, upwelling zones, downwelling zones and eddies (Alpers et al., 1991; Hovland et al., 1994). In addition, the visibility of oil spills on SAR imagery is affected by the wind speed at the sea surface. Only in a certain range of wind speeds, approximately from 2–3 m/s to 10–14 m/s, can oil spills be detected by SAR sensors (Girard-Ardhuin et al., 2005).

Detection of oil spills from SAR imagery can be divided into three steps: (1) detection of dark spots (suspicious slicks), (2) extraction of features from the detected dark spots, and (3) classification of the dark spots (oil spills/look-alikes) (Brekke & Solberg, 2005). This can be done manually or automatically. In manual detection, a trained operator has to go through the entire image, find possible oil spills and discriminate between the oil spills and the look-alikes. Though a trained operator is able to detect oil spills from SAR images with some confidence, it is time-consuming. It is also labor-intensive given the large number of SAR images that must be analyzed in a short period of time for effective oil-spill monitoring. In addition, manual detection is constrained by the knowledge and experience of operators, whose results are subjective. Thus, studies have been undertaken to develop fast, reliable and automated oil-spill detection systems (Nirchio et al., 2005; Karathanassi et al., 2006; Keramitsoglou et al., 2006; Solberg et al., 2007). Even with this work, there are still issues to be solved in

* Corresponding author.
E-mail address: junli@uwaterloo.ca (J. Li).

0034-4257/$ – see front matter © 2010 Elsevier Inc. All rights reserved.
doi:10.1016/j.rse.2010.04.009

each of the three steps identified above (Brekke & Solberg, 2005; Topouzelis, 2008).

The work presented in this paper is focused on the first step which is developing an automated approach for dark-spot detection. As a preliminary task when detecting oil spills, dark-spot detection is a critical and fundamental step prior to feature extraction and classification. Therefore, unless an oil spill can be detected at this first step, it can never be detected at a later step. Furthermore, the accuracies of feature extraction and classification greatly rely on the accuracy of dark-spot detection. In addition, dark-spot detection is traditionally the most time-consuming of the three steps. Thus, an efficient and effective dark-spot detection approach is essential for developing automated oil-spill detection systems.

Several efforts have been made to mitigate this issue in the past few years. The threshold-based algorithm is a common approach used due to its computational efficiency. With global thresholding, a universal threshold is used for the entire image. For example, in Nirchio et al. (2005), the threshold is set as the normalized radar cross section (NRCS) minus the standard deviation of the SAR image. In Chang et al. (2008), the threshold is calculated by the moment-preserving method (Tsai, 1985). With adaptive thresholding, the threshold is selected locally, within the area of a moving window. For example, in Solberg et al. (2007), the threshold that is set for dark spots is ΔdB_k below the mean value in a moving window. The value of ΔdB_k is calculated using the ratio of the standard deviation to the mean value in the local window. The thresholding is combined with a multi-scale approach and a clustering step to effectively separate dark spots from the background (i.e., the surrounding spill-free water). Other efforts to detect dark spots include the use of wavelets (Liu et al., 1997; Wu & Liu, 2003; Derrode & Mercier, 2007), fractal dimension estimation (Benelli & Garzelli, 1999; Marghany et al., 2007), marked point process (Li & Li, 2010), segmentation-based methods such as region merging (Karathanassi et al., 2006) and active contouring (Huang et al., 2005; Karantzalos & Argialas, 2008), and classification-based methods such as support vector machines (Mercier & Girard-Ardhuin, 2006) and neural networks (Topouzelis et al., 2008).

The previous methods detect a dark spot primarily through its intensity feature; i.e., the intensity in a dark spot is usually lower than the intensity in the background. However, two main difficulties occur when using the intensity domain for detection: (1) SAR imagery is highly speckled due to the constructive and destructive interferences of the reflections from surfaces of objects. Intensity values may show considerable variability, even in the neighborhood of a uniform region (Oliver & Quegan, 1998) and (2) the contrast between dark spots and the background can vary, depending on the local sea state, the type of oil spill, and the resolution and incidence angle of the SAR imagery (Topouzelis, 2008). These difficulties rule out achieving a robust and fast processing approach for dark-spot detection. In most cases, speed is sacrificed for robustness, or vice-versa in a few other cases.

The goal of the research reported in this paper is to develop a fast, robust and effective automated dark-spot detection approach that is adequate for practical oil-spill monitoring. A new approach called spatial density thresholding is proposed for achieving this goal. Apart from using the common intensity feature of dark spots, this approach further employs a spatial density feature to enhance the separability between dark spots and the background. The idea is to separate the detection process into two main steps, intensity segmentation and spatial density segmentation. A detection window is passed through the entire image. In the first step, pixels within the window are partitioned into two classes according to a certain intensity threshold. Pixels with intensities below the threshold are regarded as potential dark-spot pixels and the others are regarded as potential background pixels. In the second step, the spatial density of potential background pixels is estimated within the window. A spatial density threshold is selected. Pixels with densities below the threshold are the real dark-spot pixels, while the others with densities above the threshold are the real background pixels.

To highlight the main contribution of this paper, we refer to the whole approach as "spatial density thresholding". To avoid confusion, we refer to the algorithm used in the second step as "spatial density threshold segmentation". The power of using spatial features in image analysis has also been noticed by other scholars; e.g., Byers and Raftery (1998), Deng and Manjunath (2001) and Comaniciu and Meer (2002). An elaborate model for spatial clustering, similar to the problem addressed in the second step, has been proposed by Pavan and Pelillo (2007). However, due to the computational complexity of their model, the methods described are not fast enough for efficient dark-spot detection. In this paper, we also attempt to address the theoretical reasoning behind the suggestion that implementing spatial features can benefit SAR image analysis.

The paper is organized as follows: in Section 2, the fundamental properties of SAR imagery are presented. Section 3 contains a description of the principles behind the proposed approach and details of each step in the dark-spot detection procedures. In Section 4, the experimental results obtained using RADARSAT-1 ScanSAR intensity images are analyzed and explained. Conclusions and possibilities for future work are contained in Section 5.

2. Fundamental properties of SAR imagery

Different from other imaging systems, SAR imagery is produced by backscattered microwave signals from the surface, which can be exploited by interferometry. The classical SAR imaging model assumes that a large number of independent point scatterers with similar scattering characteristics occur within the resolution cell. When illuminated by the SAR beam, every scatterer contributes a backscattering wave with phase and amplitude change. The total returned incidence microwave is a vector sum of each individual microwave backscattered at each position, which is stated by Oliver and Quegan (1998) to be:

$$Ae^{i\phi} = \sum_{k=1}^{N} A_k e^{i\phi_k} = \sum_{k=1}^{N} A_k(\cos\phi_k + i\sin\phi_k) \quad (1)$$

where A_k is the scattering amplitude and ϕ_k is the scattering phase at position k. N is the total number of scatterers within the resolution cell. For a uniform distributed ground target, scattering behaviors of individual scatterers are identical. The amplitude of individual scatterers A_k can be assumed to be identical at different positions in the resolution cell. However, the scattering phase ϕ_k is very different within the resolution cell and can be thought of as being uniform in $[\pi, -\pi]$and independent of the amplitude A_k. Due to the constructive or destructive interference, great random fluctuation in the backscattered microwave energy can be observed as "salt-and-pepper" texture even in a uniform region. This is referred to as speckle noise in SAR imagery. Therefore, unlike system noise which occurs in the digitizing of an image, speckle is not real noise but an electromagnetic effect due to interference.

3. Methods

3.1. Principles involved

The proposed approach is motivated by the nature of the pixels' spatial distribution as observed in Fig. 1. Different symbols represent pixels with different intensities. The triangles are pixels with low intensities and the dark circles are pixels with high intensities. If the triangles are uniformly distributed in the spatial domain (Fig. 1(a)), we would deduce that the observed region is homogeneous (i.e., spill-free water) and that the triangles are speckle noise. In Fig. 1(b), however, triangles exhibit two types of spatial distribution. They

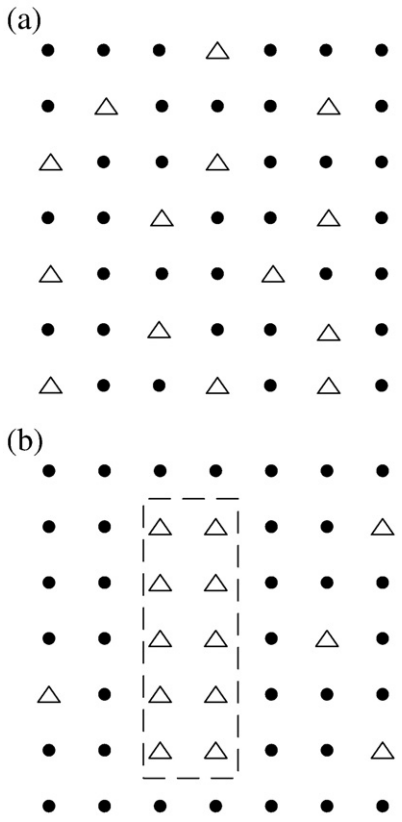

Fig. 1. Comparison of a homogeneous region and an inhomogeneous region. As described in the text, different symbols represent pixels with different intensities. (a) Homogeneous region. (b) Inhomogeneous region with a potential dark spot in the dashed box.

occur in locations where there is a high density of triangles, such as in the area contained within the dashed box. They also occur outside the dashed box where the density of triangles is much lower and interspersed with the dark circles. In the first case, we would deduce that the high density of triangles represents an area with low-intensity pixels (i.e., an oil spill) while in the second case, the triangles represent the low-intensity component of speckle noise generated over the water surface. In other words, the triangles inside the dashed box, where the density is high, are most likely to indicate the presence of a dark spot, while the other triangles are part of the background speckle noise.

How can the above observations help with developing an effective dark-spot detection approach? The Bayes criterion for detecting a dark spot states that (Oliver & Quegan, 1998):

$$P(T|x) = P(x|T)P(T) / P(x) \tag{2}$$

where x is the intensity vector, $P(T|x)$ is the posterior probability of the dark spot given the intensity, $P(x|T)$ is the likelihood probability of intensity x given the dark spot is present, and $P(T)$ is the priori probability. Similarly for the background:

$$P(B|x) = P(x|B)P(B) / P(x) \tag{3}$$

The maximum a posteriori (MAP) criterion implies that a dark spot should be considered present when:

$$\frac{P(T|x)}{P(B|x)} > 1 \tag{4}$$

from which

$$\frac{P(x|T)}{P(x|B)} > \frac{P(B)}{P(T)} \tag{5}$$

If we assume the background and the dark spot are equally likely to occur, Eq. (5) reduces to:

$$\frac{P(x|T)}{P(x|B)} > 1 \tag{6}$$

In this situation, the optimal threshold for separating the dark spot from the background in terms of the MAP criterion is where the likelihood functions of the dark spot and the background intersect (T_I as illustrated in Fig. 2). The probability of detecting a dark spot is the area marked with dashed lines (a). The corresponding probability of a false alarm in the background would be the area marked with solid lines (b). When the likelihood functions of the dark spot and the background are separate from each other, the dark spot can be easily detected from the background by simply using an appropriate intensity threshold. However, as discussed in Section 2, SAR imagery is highly speckled and the dark spot may have different contrasts relative to its background under different conditions. When the likelihood functions become similar to each other, even the optimal threshold T_I would still result in a large number of false alarms.

However, if the spatial distribution of intensity is considered, the dark spot and the background can be separated further. Before addressing this idea in detail, it is necessary to clarify our terminology to avoid any confusion. In this paper, pixels with intensities below the intensity threshold T_I are referred as "potential dark-spot pixels" or "dark pixels." Pixels with intensities above T_I are referred as "potential background pixels" or "light pixels."

It can be deduced from Eq. (6) that the probability of occurrence of a dark pixel in the dark spot (area (a) in Fig. 2) is higher than that of a dark pixel in the background (area (b) in Fig. 2). Also, according to the basic attributes of SAR imagery, described in Section 2, intensities are uniformly distributed in a uniform region. Therefore, it can be concluded that the spatial density of dark pixels is higher in a dark spot than in a background area.

If the density of dark pixels is to be estimated, the false alarms can be further separated from the real dark spots using Criterion 1:

> "The dark pixels with densities above a certain threshold T_D are the real dark-spot pixels while the pixels with densities below the threshold are the background pixels."

Similarly, the density of light pixels is expected to be lower in a dark spot than the density of pixels that occur in the background. Therefore, if the density of light pixels is to be estimated, the real dark-spot pixels that were incorrectly identified as potential background pixels can be further separated from the background using Criterion 2:

> "The light pixels with densities below a certain threshold T_D' are the real dark-spot pixels while pixels with densities above the threshold are the background pixels."

As a result, the probability of detection of a dark spot increases, while the probability of a false alarm decreases. Fig. 3(a) demonstrates the decision rule for discriminating between the dark spot and the background using Criterion 1 and Criterion 2, where the densities of both dark pixels and light pixels have to be estimated.

It can be observed that the spatial domain is fully occupied by dark and light pixels. Locations with high densities of dark pixels would definitely have low densities of light pixels. Therefore, the density estimation needs to be carried out only once (by estimating the density of either dark pixels or light pixels) in order to have the dark

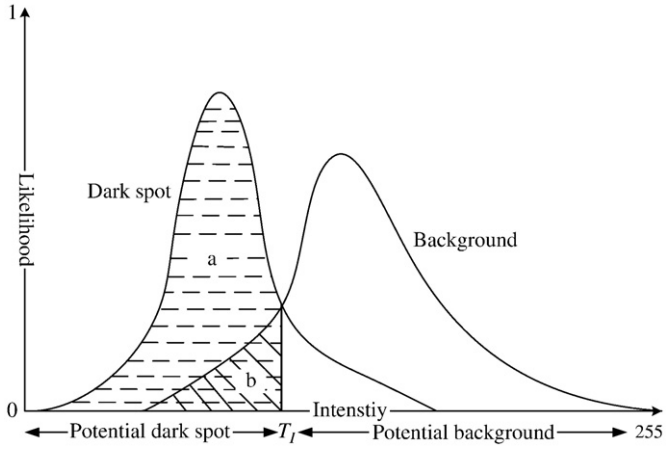

Fig. 2. Illustration of likelihood functions of a dark spot and the background. T_I is the optimal threshold for dark-spot detection according to the Bayes' rule. The area marked with dashed lines (a) is the probability of detecting a dark spot and the area marked with solid lines (b) is the probability of a false alarm in the background.

spot and the background pixels further separated. This leads to Criterion 3:

> "Locations with the densities of dark (light) pixels above (below) a certain threshold T_D (T_D') are the real dark-spot pixels while the other pixels are the background pixels."

Fig. 3(b) demonstrates a new simplified decision rule for discriminating between the dark spot and the background using Criterion 3, where spatial densities need to be estimated only once.

A new approach for dark-spot detection is proposed based on the principles described above. In this approach, a detection window is passed through the SAR image. First, an intensity threshold segmentation algorithm is implemented for each window. Pixels with intensities below the intensity threshold are regarded as potential dark-spot pixels while the others are potential background pixels. Second, the density of potential background pixels is estimated using kernel density estimation within the detection window. A spatial density threshold is selected and pixels with densities below the threshold are regarded as the real dark-spot pixels while the others are the background pixels. Third, an area and a contrast threshold are further used to eliminate any remaining false alarms. In the last step, the individual detection results are mosaicked to produce the final result. A flowchart of the procedures is illustrated in Fig. 4.

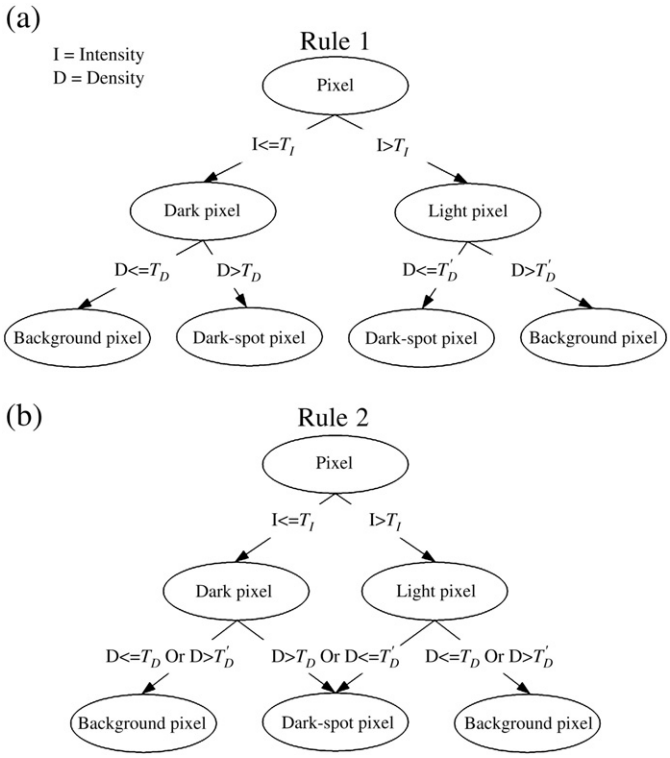

Fig. 3. Decision rules for discriminating between a dark spot and the background. (a) The decision rule (Rule 1) using Criterion 1 and Criterion 2. (b) The simplified decision rule (Rule 2) using Criterion 3.

3.2. Pre-processing

A 3×3 Gaussian filter with a standard deviation of 0.5 is used to smooth the original image. This results in a more stable intensity threshold and contrast threshold, which are discussed in the next two sections. Next, the histogram of the original image is adjusted using a piecewise linear transformation in order to enhance the contrast between the dark spot and the background. The lowest 1% of all pixel values are specified as 0, while the highest 1% are specified as 255. The remaining pixel values are stretched within the range from 0 to 255 using a linear transformation.

3.3. Intensity threshold segmentation

Since no prior knowledge is available concerning the distributions of the dark spot and the background pixels, it is not possible to find the optimal threshold value using the Bayes' rule. Instead, we use the thresholding algorithm proposed by Otsu (1979) to find an intensity threshold that maximizes the ratio of the between-class variance to the within-class variance. After the threshold is calculated, pixels with intensities above the threshold are regarded as potential background pixels while the others are potential dark-spot pixels.

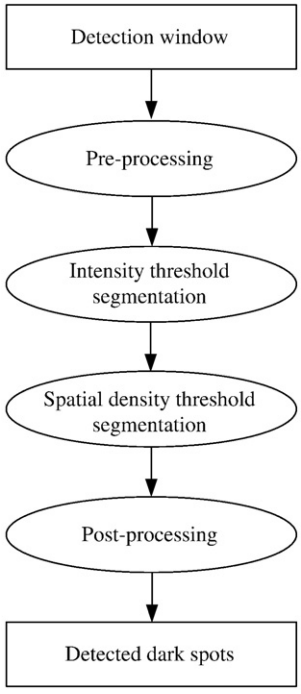

Fig. 4. Flowchart of procedures used for dark-spot detection.

3.4. Spatial density threshold segmentation

The density of potential background pixels within the detection window is estimated using kernel density estimation. Kernel density estimation, also known as the Parzen window technique in pattern recognition literature (Fukunaga, 1990), is the most popular density estimation method. Given n sample data points $x_i, i=1,...,n$ on $\boldsymbol{R}$ drawn from probability density $f(x)$, its kernel density estimator computed in the point x is given by:

$$\breve{g}(x) = \frac{1}{nt}\sum_{i=1}^{n} K\left(\frac{x-x_i}{t}\right) \tag{7}$$

where $K(x)$ is the kernel function and t is the bandwidth. $K(x)$ is required to satisfy the following two conditions:

$$\int_R K(x)du = 1 \quad \text{and} \quad K(x) \geq 0 \tag{8}$$

The most widely used kernel is the Gaussian kernel which is given by:

$$\breve{g}(x;t) = \frac{1}{n\sqrt{2\pi t^2}}\sum_{i=1}^{n} e^{-(x-x_i)^2/2t^2} \tag{9}$$

The only unknown parameter in Eq. (9) is the bandwidth t. The optimal choice of t is crucial, since the performance of $\breve{g}$ as an estimator of f depends on its value. The most widely used criterion of performance for the estimator in Eq. (9) is the mean integrated squared error (MISE):

$$\begin{aligned} MISE\{\breve{g}\}(t) &= E_f\int[\breve{g}(x;t)-f(x)]^2dx \\ &= \int\left(E_f[\breve{g}(x;t)]-f(x)\right)^2dx + \int Var_f[\breve{g}(x;t)]dx \end{aligned} \tag{10}$$

The first component of Eq. (10) is referred as point-wise bias and the second component is referred as integrated point-wise variance. Interested readers are referred to the survey of Jones et al. (1996) for a better understanding on bandwidth selection techniques.

To the best of our knowledge, the nonparametric method via diffusion mixing proposed by Botev et al. (2010) is probably the fastest and most accurate approach for kernel density estimation. As such, it is used in our study. It states that finding the optimal bandwidth for Gaussian kernel density estimator in terms of MISE criterion is equivalent to finding the optimal mixing time of the diffusion process governed by:

$$\frac{\partial}{\partial t}\breve{g}(x;t) = \frac{1}{2}\frac{\partial^2}{\partial x^2}\breve{g}(x;t), \quad x\in R, t>0\,, \tag{11}$$

with initial condition $\breve{g}(x;\ 0)=\Delta(x)=$ empirical density. For additional mathematical details on the diffusion process and the solution to Eq. (11), readers are referred to Lindeberg (1994) and Chaudhuri and Marron (2000).

To find a universal density threshold for all conditions, the estimated density is normalized using the following equation:

$$\breve{g}(x;t)_{\text{norm}} = \frac{\breve{g}(x;t)-\min(\breve{g}(x;t))}{\max(\breve{g}(x;t))-\min(\breve{g}(x;t))} \tag{12}$$

where $\max(\breve{g}(x;t))$ and $\min(\breve{g}(x;t))$ are the maximum and minimum of $\breve{g}(x;t)$, respectively. The normalized density is then transformed to the 8-bit range from 0 to 255. The selection of a density threshold is based on the idea that, if a dark spot exists, then it must have a density that is abnormal when compared with the background. Therefore, after the transformation, the densities of the real dark-spot pixels are expected to be concentrated in a narrow part of the 8-bit range, near the beginning where values are low. The threshold can thus be set accordingly. The 8-bit transformation is empirical. It was motivated by benefiting the manual threshold selection at first, because we can display the density map as an image and select the threshold visually after the 8-bit transformation. Experiments show that the threshold works well after the transformation has been performed. After the density threshold is selected, pixels with densities below the threshold are regarded as the real dark spots and pixels with densities above the threshold are the real background pixels.

It is also possible to estimate the density of potential dark-spot pixels instead of potential background pixels for spatial density threshold segmentation. However, based on the extensive experiments that we conducted, estimating the potential dark-spot pixels was found to be a little less reliable for density threshold selection than using potential background pixels.

3.5. Post-processing

During the detection process, as a result of incidental errors, some regions may have been incorrectly detected as dark spots. An area threshold T_A and a contrast threshold T_C are used to eliminate these false targets. The average contrast of a detected dark region is given by:

$$C_i = \frac{u_B-u_i}{\sigma_B} \tag{13}$$

where u_i is the average intensity of the detected dark region i, u_B is the average intensity of the background, and σ_B is the standard deviation of the intensity of the background. Only regions with an area above T_A and with an average contrast above T_C are regarded as the real dark spots. Holes inside the dark spot which are usually generated as a result of errors will be considered as the dark spot as well.

4. Experimental results

4.1. Dataset

In order to test the reliability and efficiency of the proposed approach, we obtained a test dataset from the oil-spill target database of the Integrated Satellite Tracking of Pollution (ISTOP) program at the Canadian Ice Service (CIS) of Environment Canada in Ottawa. ISTOP is a satellite surveillance program for the detection of possible discharges of oil resulting from marine transportation and offshore production. The program is supported by the Canadian Space Agency, Transport Canada, and the Canadian Coast Guard. In ISTOP, human analysts at CIS detect high potential dark spots, which could be oil spills (called anomalies), through manual interpretation of SAR images. The images used in oil-spill monitoring at CIS are RADARSAT-1 ScanSAR intensity data, with HH polarization and a spatial resolution of 50×50 m. Sub-images within the vicinity of the areas that contain anomalies were clipped to test the proposed approach. The test dataset contains 30 images with 256×256 pixels, 22 images with 512×512 pixels, 8 images with 1024×1024 pixels. This 60-image dataset contains all potential anomalies detected under a variety of sea conditions between 2006 and 2008. In addition to the analysis procedures described in Section 3, any land areas visible on the SAR images have to be masked beforehand with the aid of a vector shoreline dataset.

4.2. Experimental methods

We applied our approach to all 60 test images using the same parameters as follows: $T_D'=35, T_A=100, T_C=6.2$. These values were optimised by tuning the parameters during the experiments until the best visual detection results were achieved. The detection window

was selected to have a size of 256×256 pixels, which is considered to be a suitable size for oil-spill detection based on our experiments. False targets occupying large areas, such as low-wind areas, will not be detected using this window size. The step size for movement of the detection window is 224 pixels, with an overlap of 32×256 pixels between two consecutive steps. A visual comparison between the proposed approach and the well-known Otsu's thresholding approach (Otsu, 1979) was undertaken using a sample of test images. As described in Section 3.3, Otsu's thresholding is also used in the first step of our proposed approach. By comparing our approach with Otsu's approach, the ability of the spatial density feature to improve dark-spot detection can be examined.

To quantitatively assess the accuracy of the detection results, a reference dataset was produced by manual photo-interpretation. Due to speckle noise and varying contrasts within dark spots, however, manual interpretation can also be very difficult in certain circumstances. Thus, we checked the correctness of the computer-extracted boundaries rather than doing on-screen digitizing of the dark spots. Unless there was a reason to reject the result, we followed the computer-extracted boundaries during digitization. The computer-extracted boundaries were compared to the reference dataset. The criteria adapted from Wiedemann et al. (1998) were used for accuracy evaluation: commission error, omission error, and average difference. The commission error is defined by:

$$COM = \frac{A_E - A_{\mathrm{EinRD}}}{A_E} \tag{14}$$

where A_{EinRD} is the size of the computer-detected spots within a certain distance of the manually digitized spots and A_E is the size of the computer-detected spots. Fig. 5 gives an illustration of the commission error. The distance for measuring the commission error is set as $n=4$ pixels. The solid lines are the computer-extracted boundaries and the dashed line is the manually digitized boundary. The grey area is the one within $n=4$ pixels of the manually digitized spot and the shaded areas are the commission. Similarly, the omission error is defined by:

$$OM = \frac{A_R - A_{\mathrm{RinED}}}{A_R} \tag{15}$$

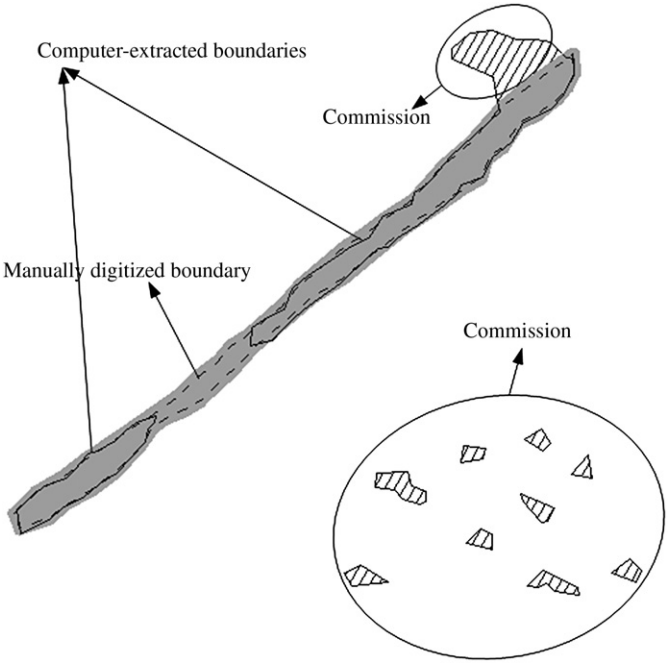

Fig. 5. Illustration of the commission error.

where A_{RinED} is the size of the manually digitized spots within a certain distance of the computer-detected spots and A_R is the size of the manually digitized spots. The portions of computer-extracted boundaries will be considered as matched, if they are within a certain distance of the manually digitized boundaries. The average difference expresses the average distance between the matched and the manually digitized boundaries, which can be calculated by:

$$AD = \sum_{i=1}^{N_B} d(EinRB_i; R) / N_B \tag{16}$$

where N_B is the number of pixels on the matched boundaries and $d(\mathrm{EinRB}_i; R)$ the shortest distance between pixel i and the manually digitized boundaries. As an additional evaluation measure, the number of false alarms per unit image can also be used; it is given by:

$$ANFA = \frac{N_{FA} \cdot N_S}{N_I} \tag{17}$$

where N_{FA} is the number of false alarms detected on the test image, N_I is the number of pixels in the test image, and N_S is the number of pixels in the unit image. The size of the unit image is set as 256×256 pixels. In addition, the computational efficiency of the proposed approach can be measured by the average computational time for a detection window.

4.3. Analysis of results

Two sample test images have been selected to illustrate the results of the proposed approach at each step. Fig. 6(a) shows the two test images after pre-processing. The image on the left contains a dark spot while the image on the right displays a homogeneous background. Fig. 6(b) shows the results of intensity threshold segmentation. The white pixels are potential background pixels and the black pixels are potential dark-spot pixels. As can be seen in Fig. 6(b), the number of false alarms is very high in the background after intensity threshold segmentation. Fig. 6(c) displays the results of the normalized density estimation of potential background pixels. Black indicates low-density areas, while white indicates high-density areas. As can be seen in the left image containing the dark spot, the density of potential background pixels is generally higher in the background than in the dark spot. Fig. 6(d) shows the results after spatial density threshold segmentation. Of note is that the number of false alarms is greatly reduced. Fig. 6(e) shows the final results after eliminating regions below the area and contrast thresholds. The extracted boundary of the dark spot (white line) is overlain on the left image. Visual inspection shows the extracted boundary and the real dark-spot boundary match quite well. In contrast, the right image containing no dark spot displays a homogeneous surface. The situation in the right image has often been neglected when two-phase classification-based methods, such as active contouring (Huang et al., 2005; Karantzalos & Argialas, 2008) and marked point process (Li & Li, 2010). It is suggested that the two-phase classification assumption is inappropriate for analyzing images without dark spots.

To test the capability of the proposed approach for detecting different types of anomalies, the whole test dataset was divided into three groups: the well-defined versus the not-well-defined, the linear versus the massive, and the homogeneous background versus the heterogeneous background. Fig. 7 illustrates the results obtained using spatial density thresholding on some typical examples. The original images, after pre-processing, are displayed in the first column. The second column shows the results obtained using Otsu's thresholding. The results of spatial density segmentation and spatial density thresholding are presented in the third and fourth columns, respectively. Displayed in the first row is a well-defined massive dark

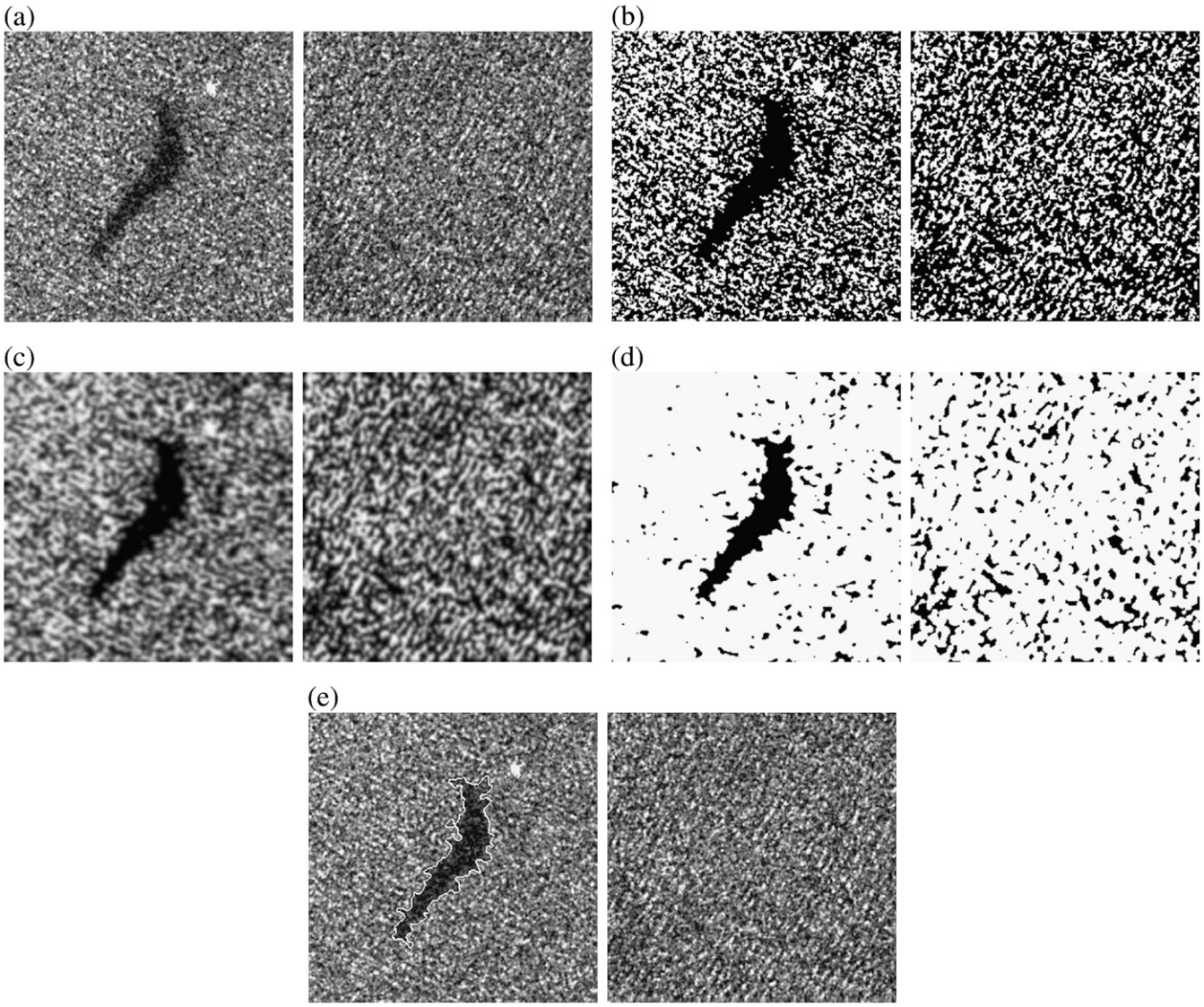

Fig. 6. Results of the proposed approach at each step in the analysis procedures. (a) Test SAR images after pre-processing. (b) Intensity threshold segmentation. (c) Normalized density estimation of potential background pixels. (d) Spatial density threshold segmentation. (e) Final results after post-processing.

spot located within a homogeneous background where the boundary between the dark spot and the surrounding water is very clear. The second row shows the detection of a not-well-defined massive dark spot within a homogeneous background. In this case, the boundary between the dark feature and the surrounding water is not well defined. In the third row, a well-defined linear dark spot can be seen located within a homogeneous background. Finally, the fourth row shows the detection of a well-defined linear dark spot that occurs within a heterogeneous background. As can be seen in Fig. 7(b), a large number of false alarms occur on the images after Otsu's thresholding. Moreover, most of the false alarms are interconnected and difficult to remove using post-processing without affecting the detection of the real dark spot. In contrast, the number of false alarms is greatly reduced after spatial density segmentation (Fig. 7 (c)). Also, the false alarms become smaller and more separated which makes them easier to eliminate with post-processing. Fig. 7 (d) shows the results after post-processing. The gray buffer is generated by manually digitizing a line with layers of $n=4$ pixels. The black line is the computer-detected boundary produced using spatial density thresholding. Visual inspection shows that the proposed approach achieves acceptable detection results under a variety of conditions.

In Table 1, the results of the quantitative accuracy assessment applied to the whole test dataset are displayed. The distance for measuring commission error, omission error, and average difference is set as $n=4$ pixels. The average commission error is 7.0% with a standard deviation of 0.11. 75% of detections have commission errors of less than 7.3%. In the worst case, a commission error of 58.6% was produced. The average omission error is 6.1% with a standard deviation of 0.13. Again, 75% of detections have omission errors less than 5.4%. In the worst case, a 55.3% omission error occurred. The mean of average difference is 0.4 pixels with a standard deviation of 0.46. In addition, the average number of false alarms is 0.5 per unit image. The average computational time for a detection window is 1.2 s on a PC-based MATLAB platform. The processor of the PC that was used is an Intel Pentium dual-core with a speed of 2.00 GHz and a RAM memory of 2.00 GB. Dark-spot detection with a 512×512 image can be completed in about 11 s. This is much faster than some of existing methods in the literature. For example, it takes about half an hour for the marked point process

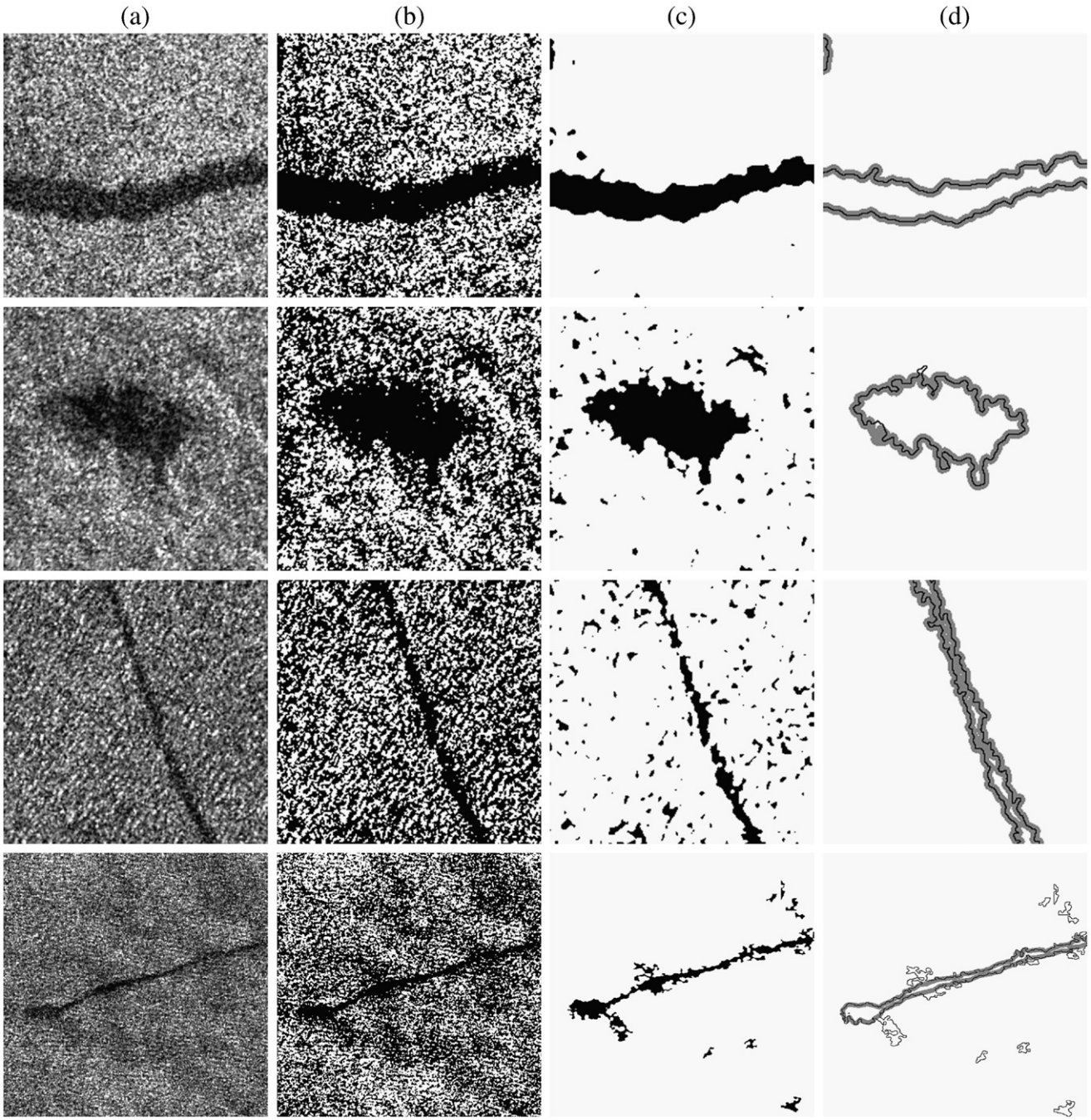

Fig. 7. Results of the proposed approach on some typical examples. (a) Original SAR images after pre-processing. (b) Otsu's thresholding. (c) Spatial density segmentation. (d) Spatial density thresholding.

to complete dark-spot detection on a 512×512 image using a PC-based MATLAB platform (Li & Li, 2010). Also, it is reported by Mercier and Girard-Ardhuin (2006) that it takes about a minute for their support vector machine method to detect a 512×512image on a 1.8-GHz Linux Laptop.

In Table 2, the accuracy assessment results for the different types of anomalies are displayed. The distance for measuring commission error, omission error, and average difference is set as $n=4$ pixels. As can be seen, spatial density thresholding achieves better results on the well-defined dark spots than the not-well-defined ones. The average commission error for the former is 5.5% versus 10.8% for the latter and the average omission error is 3.7% for the former compared to 12.1% for the latter. In addition, the approach generates more omission errors and fewer commission errors on linear dark spots than on massive dark spots. The average commission and omission errors for the linear dark spots are 9.4% and 10.5% compared to 5.4% and 2.9% for

Table 1
Statistical values of the accuracy achieved by spatial density thresholding for the whole test dataset.

	Min	Max	Mean	75th percentile	Standard deviation
Commission error	0.0000	0.5857	0.0701	0.0728	0.1104
Omission error	0.0000	0.5530	0.0605	0.0541	0.1277
Average difference	0.0000	1.8470	0.3514	0.4169	0.4645

Table 2
Mean values of the accuracies achieved by spatial density thresholding for different types of anomalies.

	Commission error	Omission error	Average difference	Number of cases
Well-defined	0.0552	0.0368	0.2838	43
Not well-defined	0.1078	0.1206	0.5224	17
Linear	0.0941	0.1053	0.4198	25
Massive	0.0540	0.0286	0.3025	35
Homogeneous	0.0546	0.0533	0.3140	54
Heterogeneous	0.2101	0.1257	0.6879	6

the massive dark spots, respectively. Furthermore, the approach produces poorer results in a heterogeneous background than in a homogeneous background. With a heterogeneous background, the average commission and omission errors are 21.0% and 12.6%, respectively. In contrast, with a homogeneous background, the average commission and omission errors are only 5.5% and 5.3%, respectively.

It is necessary to further identify the situations where poor results occurred and see why the spatial density thresholding approach failed to work correctly in those cases. Fig. 8 illustrates two typical examples. In Fig. 8(a), our approach failed because the dark spot is too thin and the contrast in some sections is too low. Human operators are able to delineate the border in Fig. 8(a) by incorporating their knowledge of linear features into the decision. In Fig. 8(b), our approach failed because the background is very heterogeneous. As can be seen, there are two types of dominate intensities in the background which cause spatial density threshold segmentation to fail. After intensity threshold segmentation, both the dark spots and the background display areas where the densities of dark pixels are high. Thus, it is difficult for the proposed approach to discriminate clearly between the dark spots and the background.

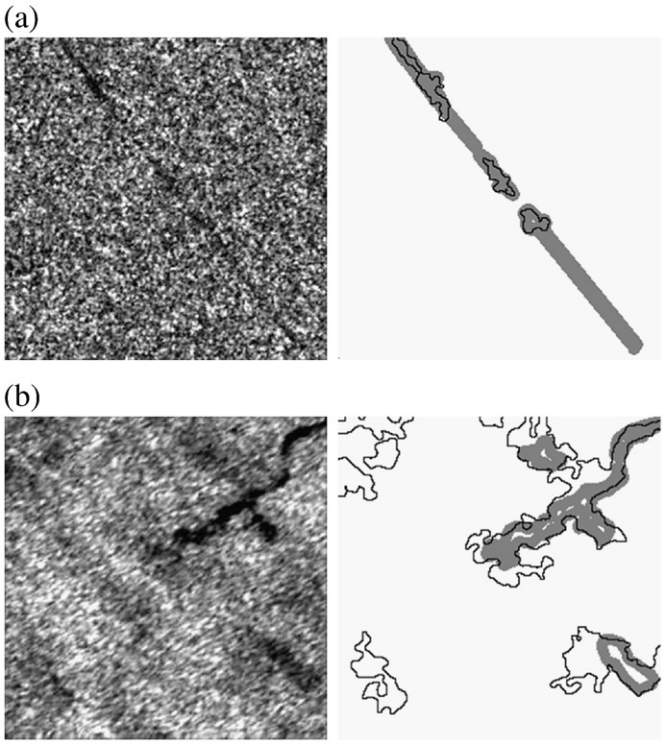

Fig. 8. Two examples of poor dark-spot detection. (a) Detection of a very thin dark spot. (b) Detection of dark spots in a very heterogeneous background.

5. Conclusions

An important first step in oil-spill monitoring is the detection of dark spots. In this paper, our analysis procedures have been focused on the spatial domain, rather than on the more frequently used intensity domain, and we have demonstrated the power of using a spatial density feature for detecting dark spots in SAR imagery. A new approach called spatial density thresholding was developed for automated dark-spot detection. To verify the effectiveness of this approach, we applied it to a test dataset containing 60 RADARSAT-1 ScanSAR intensity images which cover all potential anomaly cases detected in the ISTOP oil-spill target database between 2006 and 2008. The same parameters were used for all the test images. For the overall dataset, the average of commission error, omission error, and average difference were 7.0%, 6.1%, and 0.4 pixels, respectively. The average number of false alarms was 0.5 per unit image and the average computational time for a detection window was 1.2 s using a PC-based MATLAB platform. Using typical examples of oil spills, comparisons were made between the spatial density thresholding approach and Otsu's thresholding approach. Results demonstrated the effectiveness of spatial density thresholding. To study the detectability of different types of dark spots, we divided the test dataset into three groups. Results showed that spatial density thresholding works best when the dark spots are well-defined, massive or are embedded in a homogeneous background. It is less effective when the dark spots are not well-defined, linear, or are located within a heterogeneous background. Overall, the experimental results demonstrate that spatial density thresholding for dark-spot detection is fast, robust and effective. It has the potential to be used for automated oil-spill monitoring in an operational environment. Further research is necessary to improve the accuracy of dark-spot detection when the dark spots are not-well-defined, linear or are located in a heterogeneous background.

Acknowledgments

The authors would like to thank the Canadian Ice Service of Environment Canada for providing the RADARSAT-1 ScanSAR images, and Professor Philip Howarth and anonymous reviewers for their valuable comments and helpful suggestions for improving the manuscript.

References

Alpers, W., Wismann, V., Theis, R., Hühnerfuss, H., Bartsch, N., Moreira, J., et al. (1991). The damping of ocean surface waves by monomolecular sea slicks measured by airborne multifrequency radars during the SAXON-FPN experiment. *Proc. International Geoscience and Remote Sensing Symposium (IGARSS'91), Helsinki, Finland, 1987–1990.*

Benelli, G., & Garzelli, A. (1999). Oil spills detection in SAR images by fractal dimension estimation. *Proc. International Geoscience and Remote Sensing Symposium (IGARSS'99), Hamburg, Germany* (pp. 218—220).

Botev, Z. I., Grotowski, J. F., & Kroese, D. P. (2010). Kernel density estimation via diffusion. *Annals of Statistics*, accepted for publication.

Brekke, C., & Solberg, A. H. S. (2005). Oil spill detection by satellite remote sensing. *Remote Sensing of Environment*, *95*(1), 1—13.

Byers, S., & Raftery, A. E. (1998). Nearest-neighbor clutter removal for estimating features in spatial point processes. *Journal of the American Statistical Association*, *93*, 577—584.

Chang, L., Tang, Z. S., Chang, S. H., & Chang, Y. L. (2008). A region-based GLRT detection of oil spills in SAR images. *Pattern Recognition Letters*, *29*(14), 1915—1923.

Chaudhuri, P., & Marron, J. S. (2000). Scale space view of curve estimation. *The Annals of Statistics*, *28*(2), 408—428.

Comaniciu, D., & Meer, P. (2002). Mean shift: a robust approach toward feature space analysis. *IEEE Transactions on Pattern Analysis and Machine Intelligence*, *24*(5), 1—18.

Deng, Y., & Manjunath, B. S. (2001). Unsupervised segmentation of color–texture regions in images and video. *IEEE Transactions on Pattern Analysis and Machine Intelligence*, *23*(8), 800—810.

Derrode, S., & Mercier, G. (2007). Unsupervised multiscale oil slick segmentation from SAR images using a vector HMC model. *Pattern Recognition*, *40*, 1135—1147.

Fukunaga, K. (1990). *Introduction to statistical pattern recognition*, 2nd edition San Diego, CA: Academic Press Professional.

Girard-Ardhuin, F., Mercier, G., Collard, F., & Garello, R. (2005). Operational oil-slick characterization by SAR imagery and synergistic data. *IEEE Transactions on Geoscience and Remote Sensing*, *3*, 487−495.

Hovland, H. A., Johannessen, J. A., & Digranes, G. (1994). Slick detection in SAR images. *Proc. International Geoscience and Remote Sensing Symposium (IGARSS 94), Pasadena, CA, USA* (pp. 2038−2040).

Huang, B., Li, H., & Huang, X. (2005). A level set method for oil slick segmentation in SAR images. *International Journal of Remote Sensing*, *26*, 1145−1156.

Jones, M. C., Marron, J. S., & Sheather, S. J. (1996). A brief survey of bandwidth selection for density estimation. *Journal of the American Statistical Association*, *91*, 401−407.

Karantzalos, K., & Argialas, D. (2008). Automatic detection and tracking of oil spills in SAR imagery with level set segmentation. *International Journal of Remote Sensing*, *29*(21), 6281−6296.

Karathanassi, V., Topouzelis, K., Pavlakis, P., & Rokos, D. (2006). An object-oriented methodology to detect oil spills. *International Journal of Remote Sensing*, *27*, 5235−5251.

Keramitsoglou, I., Cartalis, C., & Kiranoudis, C. (2006). Automatic identification of oil spills on satellite images. *Environmental Modeling & Software*, *21*, 640−652.

Li, Y., & Li, J. (2010). Oil spill detection from SAR intensity image using marked point process. *Remote Sensing of Environment*. doi:10.1016/j.rse.2010.02.013.

Lindeberg, T. (1994). *Scale space theory in computer vision.* Boston: Kluwer.

Liu, A. K., Peng, C. Y., & Chang, S. Y. -S. (1997). Wavelet analysis of satellite images for coastal watch. *IEEE Journal of Ocean Engineering*, *22*, 9−17.

Marghany, M., Hashim, M., & Cracknell, A. P. (2007). Fractal dimension algorithm for detecting oil spills using Radarsat-1 SAR. In O. Gervasi & M. Gavrilova (Eds.), *Lecture notes in computer science (LNCS) 4705* (pp. 1054−1062). Berlin: Springer.

Mercier, G., & Girard-Ardhuin, F. (2006). Partially supervised oil-slick detection by SAR imagery using kernel expansion. *IEEE Transactions on Geoscience and Remote Sensing*, *44*(10), 2839−2846.

Nirchio, F., Sorgente, M., Giancaspro, A., Biamino, W., Parisato, E., Ravera, R., et al. (2005). Automatic detection of oil spills from SAR images. *International Journal of Remote Sensing*, *26*(6), 1157−1174.

Oliver, C., & Quegan, S. (1998). *Understanding synthetic aperture radar images.* London: Artech House.

Otsu, N. (1979). A threshold selection method from gray-level histograms. *IEEE Transactions on Systems, Man, and Cybernetics*, *9*(1), 62−66.

Pavan, M., & Pelillo, M. (2007). Dominant sets and pairwise clustering. *IEEE Transactions on Pattern Analysis and Machine Intelligence*, *29*(1), 167−172.

Solberg, A. H. S., Brekke, C., & Husøy, P. O. (2007). Oil spill detection in Radarsat and Envisat SAR images. *IEEE Transactions on Geoscience and Remote Sensing*, *45*(3), 746−755.

Topouzelis, K. (2008). Oil spill detection by SAR images: dark formation detection, feature extraction and classification. *Sensors*, *8*, 6642−6659.

Topouzelis, K., Karathanassi, V., Pavlakis, P., & Rokos, D. (2008). Dark formation detection using neural networks. *International Journal of Remote Sensing*, *29*, 4705−4720.

Tsai, W. H. (1985). Moment-preserving thresholding: a new approach. *Computer Vision, Graphics, and Image Processing*, *29*, 377−393.

Wiedemann, C., Heipke, C., Mayer, H., & Jamet, O. (1998). Empirical evaluation of automatically extracted road Axes. *CVPR workshop on empirical evaluation methods in computer vision* (pp. 172−187).

Wu, S. Y., & Liu, A. K. (2003). Towards an automated ocean feature detection, extraction and classification scheme for SAR imagery. *International Journal of Remote Sensing*, *24*, 935−951.